Supporting information to "Frequent occurrence of newly formed aerosol particles over wide geographical areas in the Arctic free troposphere and atmospheric boundary layer"

David J. Simon[1], Jonas Schaefer[1], Jörg Hartmann[2], Benjamin Kirbus[3], Joshua Müller[3], Markus Hartmann[1], Bruno Wetzel[1], Laura Köhler[2], Anna-Marie Jörss[2], Kay Weinhold[1], Andreas Herber[2], Zsófia Jurányi[2], Silvia Henning[1], Gregory C. Roberts[4], Manfred Wendisch[3], Mira L. Pöhlker[1,3], and Frank Stratmann[1]

[1]Atmospheric Microphysics Department, Leibniz Institute for Tropospheric Research, Leipzig, Germany
[2]Alfred Wegener Institute, Helmholtz Centre for Polar and Marine Research, Bremerhaven, Germany
[3]Leipzig Institute for Meteorology, Leipzig University, Leipzig, Germany
[4]Scripps Institution of Oceanography, La Jolla, CA, USA

Correspondence: David J. Simon (simon@tropos.de)

S1 Research flights during the aircraft measurement campaign

Fig. S1 shows the flight tracks of all eleven research flights (RFs) conducted with the Polar 6 (P6) aircraft during the measurement campaign "Boundary layer and Aerosol and Cloud Study in the Arctic, based on aircraft and T-Bird Measurements II" (BACSAM II).

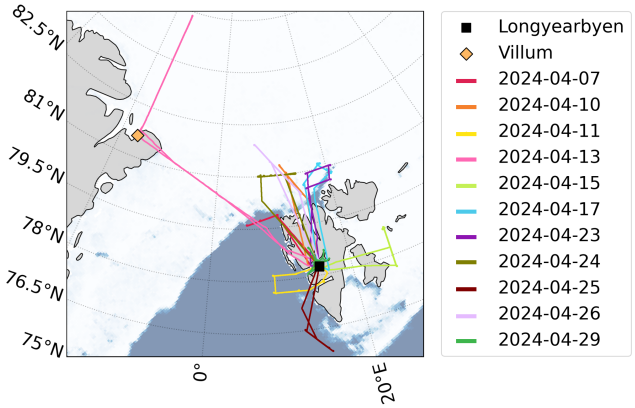

Figure S1. Flight tracks of all research flights during BACSAM II. The sea ice concentration is shown exemplary for 15 April 2024. The corresponding sea ice data were retrieved from www.seaice.uni-bremen.de (Spreen et al., 2008).

S2 Detection and categorization of newly formed particles

S2.1 Detection of newly formed particles

As outlined in the main text (Sect. 2.2), we fitted log-normal functions featuring one, two, or three modes to the mobility particle size spectrometer-measured (MPSS-measured) particle number size distribution (PNSD) data. If the fitting procedure returned a mode featuring a maximum below 10 nm, i.e., below the lower size limit of the MPSS, we consider the measurement to indicate the presence of newly formed particles. The detection of newly formed particles was verified by visual inspection of the fitted PNSDs. As outlined in the main text, MPSS measurements carried out during ascents and descents were excluded from the quantitative analysis. Fig. S2 shows examples of three fitted PNSDs, with the data displayed in Fig. S2a and Fig. S2c indicating the presence of newly formed particles, and the data in Fig. S2b the absence of newly formed particles.

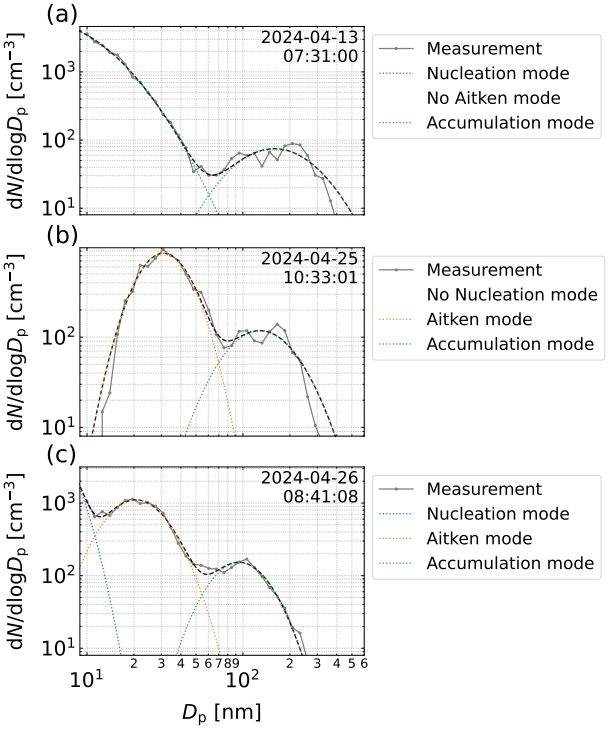

Figure S2. Examples of MPSS-measured PNSDs, showing nucleation and/or Aitken, and accumulation modes. The PNSDs shown in the panels (a) and (c) are considered as indicative for newly formed particles, while the measurement displayed in panel (b) shows no indication for newly formed particles.

S2.2 Categorization of newly formed particles

The MPSS-measured PNSDs indicative of newly formed particles were categorized according to three environmental conditions for which they were mainly observed, i.e., newly formed particles detected in the free troposphere (Sect. 3.2 in the

main text), in the atmospheric boundary layer (ABL) over sea ice (Sect. 3.3), and in the vicinity of clouds (Sect. 3.4). Fig. S3 shows the median PNSDs and corresponding interquartile ranges of all MPSS measurements per category. For convenience, the PNSDs are shown on both a logarithmic (upper panel) and linear axis (lower panel).

For approximately 14 % of all PNSDs featuring newly formed particles, the prevailing conditions could not unambiguously be identified. These include flight sections during which clouds were present, but in contrast to the newly formed particles classified as "in the vicinity of clouds", we did not fly directly at cloud top or base, respectively. Contained in the 14 % of unclassified cases are also sections at rather low altitudes (60 - 300 m, see Fig. 2b in the main text) over ocean, which were at least partly carried out inside the marine ABL. Here, either clouds were present as well, or sea ice floes were visible in addition to open sea areas, preventing the clear identification of the potential precursor source (open sea or sea ice). Consequently, we cannot rule out that the open ocean acted as source of precursor gases (e.g., dimethyl sulfide (DMS), Willis et al., 2018) leading to newly formed particles in some of the regions targeted during our campaign, but, in contrast to the three other cases investigated, no clear observations of newly formed particles over open ocean were made.

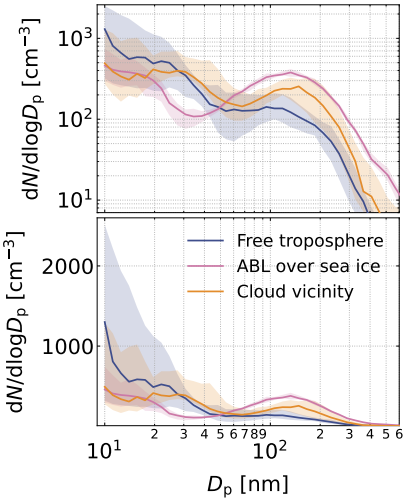

Figure S3. Median PNSD of all cases of newly formed particles associated with one of the three environments described in the main text and discussed in detail in the respective sections 3.2 (free troposphere), 3.3 (ABL over sea ice), and 3.4 (cloud vicinity). The shaded areas represent the interquartile ranges.

S3 Thermodynamic conditions prevailing during the occurrence of newly formed particles

In Fig. S4, relative frequencies of occurrence of measured temperature and relative humidity pairs (T-RH pairs) are plotted in a temperature vs. relative humidity plane. The relative frequencies were calculated considering the number of measured T-RH pairs during the presence of newly formed particles (Fig. S4a, 37452 pairs) and considering the number of T-RH pairs measured during the absence of newly formed particle (Fig. S4b, 116891 pairs). The histograms shown in Fig. S4c-e

were calculated by normalizing the T-RH data pairs recorded only during observations of newly formed particles in the free troposphere (Fig. S4c), only during observations of newly formed particles in the ABL over sea ice (Fig. S4d), and only during observations of newly formed particles in the vicinity of clouds (Fig. S4e) by the data recorded during all observations of newly formed particles combined. That is, the normalization is the same as for the histogram depicted in Fig. S4a. The dotted horizontal and vertical lines separating the subplot into four quadrants in Fig. S4 are plotted to guide the eyes.

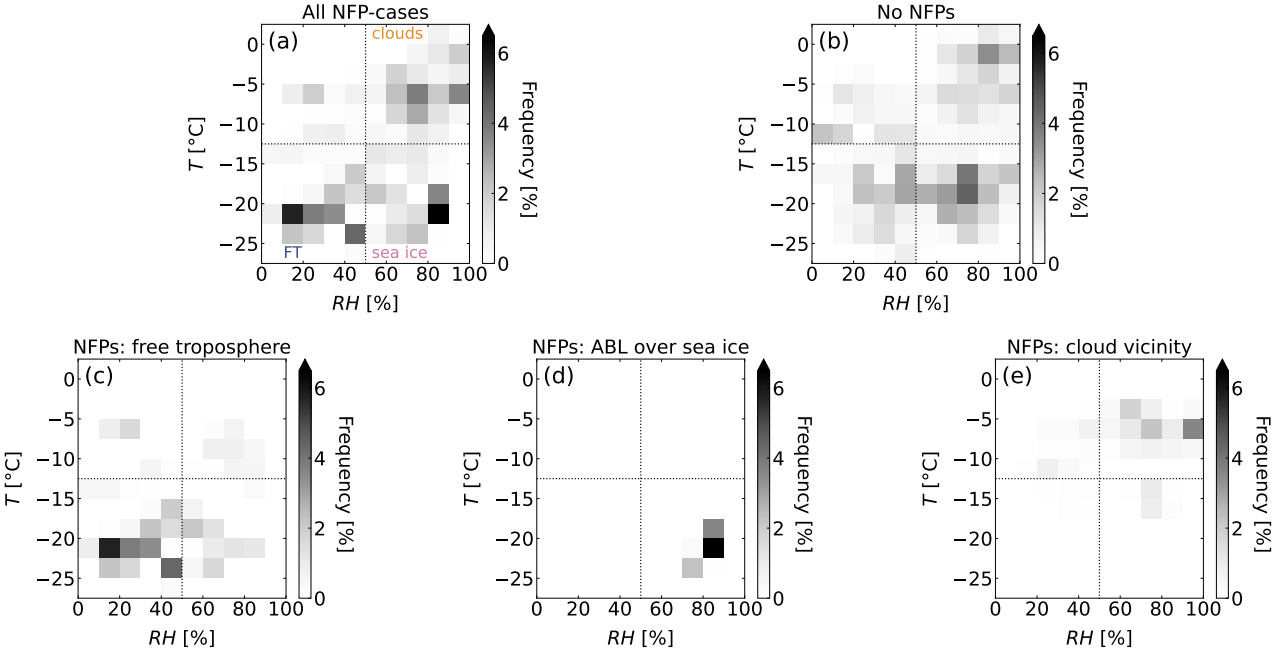

Figure S4. Temperature and relative humidity conditions during **(a)** newly formed particle-cases (NFP-cases) and **(b)** non-NFP-cases. The labels "FT", "sea ice", and "clouds" in panel (a) denote that within the corresponding quadrant, the measured temperature and relative humidity values are predominantly associated with newly formed particles observed in the free troposphere, the ABL over sea ice, and cloud vicinity, respectively. The second row depicts temperature and relative humidity during the occurrence of newly formed particles **(c)** in the free troposphere, **(d)** the ABL over sea ice, **(e)**, and the vicinity of clouds

From Fig. S4, a clear pattern becomes visible. The data show three main clusters in the relative frequency distribution of temperature and humidity conditions during observations of newly formed particles (Fig. S4a), while the frequency distribution of T-RH pairs measured during the absence of newly formed particles is broader, with fewer pronounced features (Fig. S4b). The peaks in Fig. S4a, i.e., in the T-RH distribution measured during observations of newly formed particles, correspond to the different environmental scenarios under which newly formed particles were detected. Newly formed particles in the free troposphere were predominantly associated with cold and dry conditions (lower left quadrant in Fig. S4a, Fig. S4c). Newly formed particles in the ABL over sea ice occurred during cold and humid conditions (lower right quadrant in Fig. S4a, Fig. S4d). For newly formed particles detected in the vicinity of clouds, relatively warm and humid conditions prevailed (upper right quadrant in Fig. S4a, Fig. S4e). As mentioned in Sect. 3.1 in the main text and in supporting information (SI) Sect. S2.2,

we found no clear indications for newly formed particles inside the ABL over open ocean during our campaign. T-RH data measured during such observations would likely also feature warm and humid conditions, similar to the data recorded during observations of newly formed particles in the vicinity of clouds. Altogether, these results show that newly formed particles observed during BACSAM II seem to be associated with distinct thermodynamic conditions, which correspond to the different atmospheric scenarios for which newly formed particles were encountered, i.e., free tropospheric newly formed particles, newly formed particles inside the ABL over sea ice, and newly formed particles in the vicinity of clouds. These data provide important information on boundary conditions for laboratory experiments and modeling studies, both of which could facilitate the identification of nucleation mechanisms that might have lead to the presence of newly formed particles, and, furthermore, to assess the broader atmospheric (climate) impact of newly formed particles occurring throughout the lower Arctic troposphere.

S4 New and recently formed particles in the free troposphere

Fig. S5 shows the median PNSD and corresponding interquartile range of all PNSD-measurements indicative of newly formed particles during the transit to Villum research station in the free troposphere (13 April 2024, RF04, Sect. 3.2 in the main text). These data were recorded during the time period 6:23 to 7:07 UTC and 7:17 to 7:40 UTC.

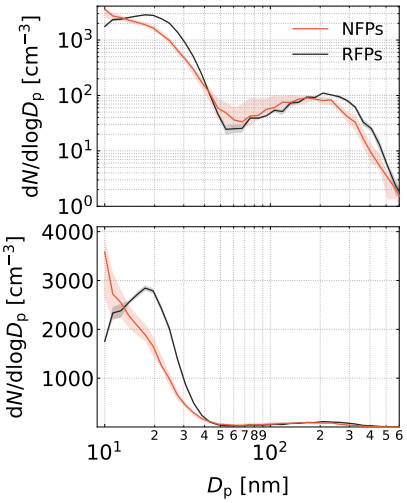

Figure S5. Median PNSD of measurements indicative of newly formed particles (NFPs) and recently formed particles (RPFs, solid lines) observed on 13 April 2024 during the transit from Longyearbyen to Villum Research Station (case study in the free troposphere). The shaded areas represent the interquartile ranges.

Two PNSDs measured in the time period from 7:07 to 7:17 UTC peaked at about 18 nm and showed no indications concerning a mode featuring a maximum below 10 nm (Fig. S5). According to our criteria defined above, these PNSDs are not considered as indicative for newly formed particles. We rather interpret them as steming from "recent particle formation" (RPF), since

the small particle sizes still suggest that these particles must originate from secondary particle production (e.g., Kulmala et al., 2004). Such recently formed particles are excluded from further analysis and we here focus solely on newly formed particles. Investigating recently formed particles in further detail is beyond the scope of this paper.

S5 Newly formed particles in the atmospheric boundary layer over sea ice

S5.1 Sea ice conditions

To illustrate the sea ice conditions prevailing in the target region east of Svalbard between waypoint 1 (WP1) and WP3 on 15 April 2024 (RF05, Sect. 3.3 in the main text), Fig. S6 displays examples of fisheye camera images facing downward from the P6 aircraft during the legs inside the ABL. Leads and cracks in the sea ice are visible.

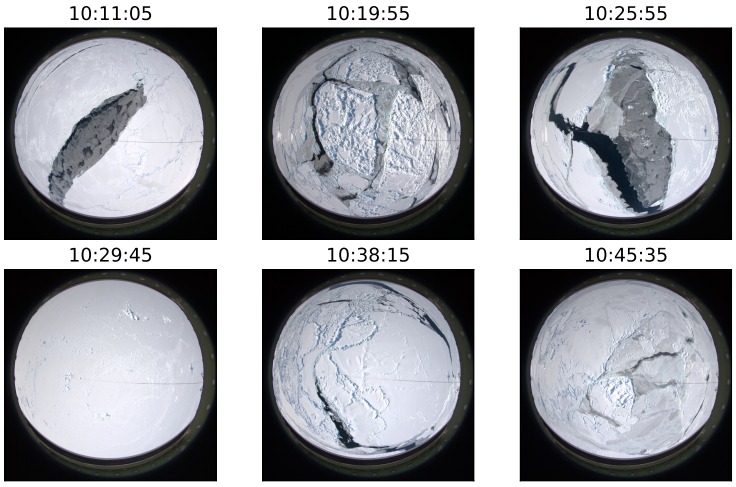

Figure S6. Sea ice conditions during RF05 on 15 April 2024 (case study in the ABL over sea ice). The title denotes the time in UTC.

S5.2 Vertical profile

From the inversion observed in the vertical profiles of potential temperature (Θ) between WP1 and WP3, we determine the ABL height (Fig. S7). The solid line in Fig. S7 shows the mean Θ-profile averaged over the four ascents/descents at WP1, WP2, and WP3 (see Fig.7a in the main text). The shaded area represents the standard deviation and thus the variability between the individual ascents/descents. The data have been grouped into altitude bins with a width of 20 m before averaging. The markers with errorbars show mean values and standard deviations derived from the measurements during the horizontal legs. The horizontal dashed lines represent the average aircraft altitude during these low-level legs (at $\approx 70\,\mathrm{m}$ and $\approx 155\,\mathrm{m}$) close to the surface inside the ABL ($h_{\mathrm{P6,\,inside\,BL}}$) and the high-level leg above the ABL in the free troposphere ($h_{\mathrm{P6,\,outside\,BL}} \approx 850\,\mathrm{m}$). In Fig. S7, an inversion at an altitude of about 170 m can be identified for the target region.

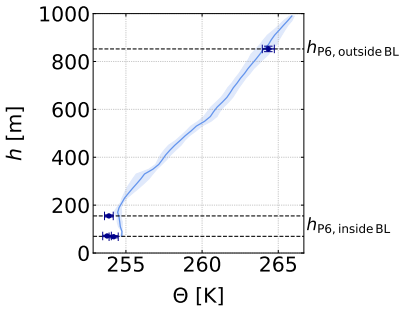

Figure S7. Mean vertical profile of potential temperature for the case study in the ABL over sea ice on 15 April 2024, derived from the ascents/descents (solid line). The shaded area represents the standard deviation. The markers with errorbars show mean values and standard deviations derived from the measurements during the horizontal legs. The horizontal dashed lines illustrate the average aircraft altitude during these legs.

S5.3 Particle number size distributions

Fig. S8 shows the median PNSDs measured during the three consecutive legs carried out in the same area and at constant altitude between WP1 and WP3 (see Fig. 7a in the main text) inside the ABL over sea ice. ABL 1 refers to the first leg flown inside the ABL at an altitude of $\approx 70\,\mathrm{m}$ (10:15 to 10:47 UTC), ABL 2 to the second leg at $\approx 155\,\mathrm{m}$ (10:58 to 11:25 UTC), and ABL 3 to the third leg, again at $\approx 70\,\mathrm{m}$ (12:13 to 12:43 UTC). The decrease with time of the number concentration in the size range below 20 nm is clearly visible.

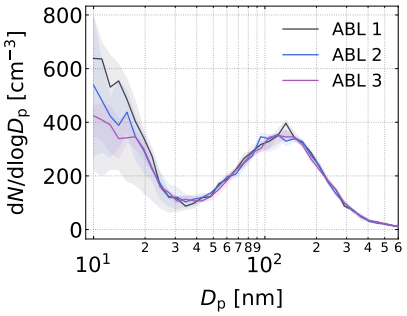

Figure S8. Median PNSDs (solid lines) and corresponding interquartile ranges (shaded areas) for the legs at $\approx 70\,\mathrm{m}$ (ABL 1 and ABL 3) and $\approx 155\,\mathrm{m}$ (ABL 2) inside the ABL over sea ice on 15 April 2024.

S6 Newly formed particles in the vicinity of clouds

S6.1 Sea ice conditions

To illustrate the sea ice conditions prevailing in the target region north of Svalbard between WP1 and WP2 on 24 April 2024 (RF08, Sect. 3.4 in the main text), Fig. S9 displays examples of fisheye camera images facing downward from the P6 aircraft during the leg at cloud base. Leads and cracks in the sea ice are visible.

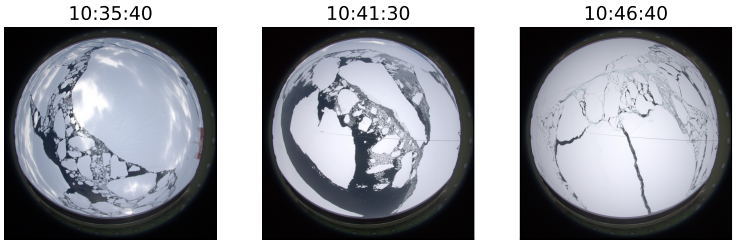

Figure S9. Sea ice conditions during RF08 on 24 April 2024 (case study in the vicinity of clouds). The title denotes the time in UTC.

S6.2 Vertical profiles

For the case study on newly formed particles in the vicinity of clouds, the ascent through cloud (10:52 to 10:58 UTC, see Fig. 10a in the main text) is excluded from analysis with respect to the aerosol particle measurements, because erroneous measurements due to icing of the aerosol inlet and/or droplet shattering cannot be ruled out (Weber et al., 1998). Nevertheless, temperature and pressure data recorded during the ascent can with caution be used to determine vertical profiles of potential temperature to investigate the stratification in the target region. In Fig. S10, we show the potential temperature derived from these data collected during the ascent through cloud (see Fig. 10a in the main text). Directly in the target region between WP1 and WP2 (see Fig. 9a in the main text), no vertical profiling down to the lowest possible flight altitude was carried out. Therefore, in addition, the potential temperature derived from a vertical profile down to $\approx 80\,\mathrm{m}$, which was conducted after passing WP2 and while returning towards the sea ice edge (see Fig. 9(a) in the main text), is depicted in Fig. S10. Here, the solid line represents the mean, averaged over ascent and descent, and the shaded area the corresponding standard deviation. Additionally, we show the potential temperature profile in the target region between WP1 and WP2 based on Copernicus Arctic Regional Reanalysis (CARRA) data. Cloud top and base, illustrated by the shaded gray area representing the cloud in Fig. S10, were determined from the profile of potential temperature and from in situ video data. Both CARRA and in situ data show an inversion below the cloud, which suggests that in the area probed between WP1 and WP2, the clouds were decoupled from the surface.

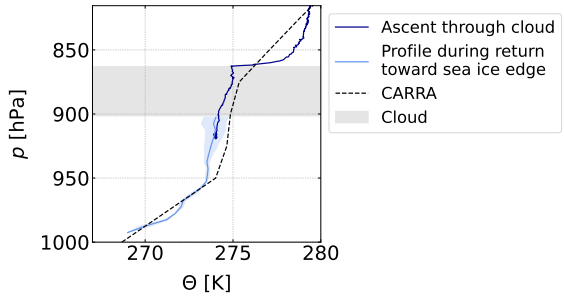

Figure S10. Vertical profile of potential temperature for the case study in the vicinity of clouds on 24 April 2024, derived from in situ data collected during ascents/descents (solid lines) as well as based on CARRA reanalysis data (dashed line).

S6.3 Cloud top radiative cooling

We further utilize the ascent through the cloud to determine the radiative heating/cooling rates in an atmospheric layer between two flight altitudes, with $z_{\mathrm{bottom/top}}$ denoting the altitudes at the bottom/top of this layer (Lonardi et al., 2024). Following Lonardi et al. (2024), we calculate the heating/cooling rates as

$$\zeta = \frac{1}{\rho c_{\mathrm{p}}} \frac{F_{\mathrm{net}}(z_{\mathrm{top}}) - F_{\mathrm{net}}(z_{\mathrm{bottom}})}{z_{\mathrm{top}} - z_{\mathrm{bottom}}}, \tag{1}$$

where ρ and c_{p} are density and specific heat capacity at constant pressure of air, and $F_{\mathrm{net}}(z)$ the net thermal irradiance at flight altitude z. Positive/negative values in ζ indicate radiative heating/cooling (Lonardi et al., 2024). The heating/cooling rates are plotted in Fig. S11, which shows a sharp minium at about 1150 m, i.e., radiative cooling at the cloud top.

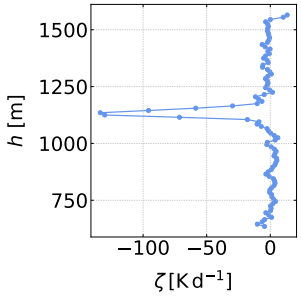

Figure S11. Radiative heating/cooling rates for the case study in the vicinity of clouds on 24 April 2024, determined from the ascent through cloud.

Acknowledgements. We gratefully acknowledge the funding by the Deutsche Forschungsgemeinschaft (DFG, German Research Foundation) – Project Number 268020496 – TRR 172, within the framework of the Transregional Collaborative Research Center "ArctiC Amplification:

Climate Relevant Atmospheric and SurfaCe Processes, and Feedback Mechanisms (AC)^3", as well as the support of the Alfred-Wegener-Institute, Helmholtz Centre for Polar and Marine Research through grant number AWI_PA_02172. The authors used a large language model (ChatGPT by OpenAI) solely to support coding tasks; all scientific reasoning, methodological decisions, analyses, and conclusions were developed independently by the authors.

References

Kulmala, M., Vehkamäki, H., Petäjä, T., Dal Maso, M., Lauri, A., Kerminen, V.-M., Birmili, W., and McMurry, P.: Formation and growth rates of ultrafine atmospheric particles: a review of observations, Journal of Aerosol Science, 35, 143–176, https://doi.org/10.1016/j.jaerosci.2003.10.003, 2004.

Lonardi, M., Akansu, E. F., Ehrlich, A., Mazzola, M., Pilz, C., Shupe, M. D., Siebert, H., and Wendisch, M.: Tethered balloon-borne observations of thermal-infrared irradiance and cooling rate profiles in the Arctic atmospheric boundary layer, Atmospheric Chemistry and Physics, 24, 1961–1978, https://doi.org/10.5194/acp-24-1961-2024, 2024.

Spreen, G., Kaleschke, L., and Heygster, G.: Sea ice remote sensing using AMSR-E 89-GHz channels, Journal of Geophysical Research: Oceans, 113, https://doi.org/10.1029/2005JC003384, 2008.

Weber, R., Clarke, A., Litchy, M., Li, J., Kok, G., Schillawski, R., and McMurry, P.: Spurious aerosol measurements when sampling from aircraft in the vicinity of clouds, Journal of Geophysical Research: Atmospheres, 103, 28 337–28 346, https://doi.org/10.1029/98JD02086, 1998.

Willis, M. D., Leaitch, W. R., and Abbatt, J. P.: Processes controlling the composition and abundance of Arctic aerosol, Reviews of Geophysics, 56, 621–671, https://doi.org/10.1029/2018RG000602, 2018.